13. H. Rauch, S. A. Werner, *Neutron Interferometry: Lessons in Experimental Quantum Mechanics* (Calderon Press, Oxford, UK, 2000).
14. S. Dürr, T. Nonn, G. Rempe, *Nature* **395**, 33–37 (1998).
15. S.-Y. Lan *et al.*, *Science* **339**, 554–557 (2013).
16. W. P. Schleich, D. M. Greenberger, E. M. Rasel, *Phys. Rev. Lett.* **110**, 010401 (2013).
17. S. Peil, C. R. Ekstrom, *Phys. Rev. A* **89**, 014101 (2014).
18. Materials and methods are available as supplementary materials on *Science* Online.
19. S. Machluf, Y. Japha, R. Folman, *Nat. Commun.* **4**, 2424 (2013).
20. R. Penrose, *The Emperor's New Mind: Concerning Computers, Minds, and the Laws of Physics* (Oxford Univ. Press, New York, 1989), chap. 6.
21. L. Diósi, *J. Phys. Conf. Ser.* **442**, 012001 (2013).
22. A. Bassi, K. Lochan, S. Satin, T. P. Singh, H. Ulbricht, *Rev. Mod. Phys.* **85**, 471–527 (2013).
23. Lee Smolin, *Time Reborn* (Mariner Books, Wilmington, MA, 2014).

ACKNOWLEDGMENTS

We thank Z. Binshtok, S. Zhou, M. Keil, D. Groswasser, Y. Bar-Haim, and M. Givon for their assistance and the Ben-Gurion University of the Negev nanofabrication facility for providing the high-quality chip. This work is funded in part by the Israeli Science Foundation, the European Commission "MatterWave"' consortium (FP7-ICT-601180), and the German-Israeli DIP project (Quantum phenomena in hybrid systems) supported by the Deutsche Forschungsgemeinschaft. We also acknowledge support from the program for outstanding postdoctoral researchers of the Israeli Council for Higher Education and from the Ministry of Immigrant Absorption (Israel). D.R. thanks the John Templeton Foundation (Project ID 43297) and the Israel Science Foundation (grant 1190/13) for support. The opinions expressed in this publication do not necessarily reflect the views of the John Templeton Foundation.

SUPPLEMENTARY MATERIALS

www.sciencemag.org/content/349/6253/1205/suppl/DC1
Materials and Methods
Supplementary Text
Figs. S1 to S4
References (*24*–*28*)

27 May 2015; accepted 21 July 2015
Published online 6 August 2015
10.1126/science.aac6498

ELECTROCHEMISTRY

Covalent organic frameworks comprising cobalt porphyrins for catalytic CO_2 reduction in water

Song Lin,[1,2]* Christian S. Diercks,[1,3]* Yue-Biao Zhang,[1,3,4]* Nikolay Kornienko,[1] Eva M. Nichols,[1,2] Yingbo Zhao,[1] Aubrey R. Paris,[1] Dohyung Kim,[5] Peidong Yang,[1,3,5,6] Omar M. Yaghi,[1,3,6,7]† Christopher J. Chang[1,2,8,9]†

Conversion of carbon dioxide (CO_2) to carbon monoxide (CO) and other value-added carbon products is an important challenge for clean energy research. Here we report modular optimization of covalent organic frameworks (COFs), in which the building units are cobalt porphyrin catalysts linked by organic struts through imine bonds, to prepare a catalytic material for aqueous electrochemical reduction of CO_2 to CO. The catalysts exhibit high Faradaic efficiency (90%) and turnover numbers (up to 290,000, with initial turnover frequency of 9400 $hour^{-1}$) at pH 7 with an overpotential of −0.55 volts, equivalent to a 26-fold improvement in activity compared with the molecular cobalt complex, with no degradation over 24 hours. X-ray absorption data reveal the influence of the COF environment on the electronic structure of the catalytic cobalt centers.

Global energy demands and climate change underpin broad interest in the sustainable reductive transformation of carbon dioxide (CO_2) to value-added carbon products such as carbon monoxide (CO) (*1*, *2*). Electrolytic approaches benefit from using water as the reaction medium, as it is a cheap, abundant, and environmentally benign solvent that facilitates proton and electron transfer (*3*, *4*). However, the competitive and often kinetically favored off-pathway reduction of water itself to hydrogen must be avoided. In this context, molecular catalysts for electrochemical CO_2 conversions can be systematically tuned to achieve high activity and selectivity over proton reduction (*5*–*13*), but they typically require organic media to achieve optimal selectivity and/or stability, often to maximize solubility and minimize water- or proton-induced catalyst degradation and/or hydrogen production. In contrast, heterogeneous catalysts are often stable in water, but optimizing their activity through structural changes at a molecular level remains a substantial challenge (*14*–*19*). Against this backdrop, we sought to investigate crystalline porous frameworks—specifically, covalent organic frameworks (COFs) (*20*–*22*)—as tunable materials for electrocatalysis. We reasoned that such materials could potentially combine advantages of both molecular and heterogeneous catalysts: (i) Construction with molecular building blocks would enable precise manipulation of the spatial arrangement of catalytic centers within the predetermined COF structure (*23*); (ii) the frameworks could be expanded and functionalized without changing the underlying topology of the structure (*24*, *25*); and (iii) the conserved pore environment around the active sites within the COF could be tuned electronically and sterically (*26*) while providing ready access for the substrate (*27*–*32*) (Fig. 1). Moreover, these crystalline porous frameworks offer the possibility to perform multivariate synthesis, in which topologically identical and yet functionally modified building blocks can be introduced into the structure. This approach can potentially give rise to materials with emergent properties that are greater than the sum of the individual molecular parts, because one can predictably prepare a topologically ordered framework yet introduce heterogeneity in the number and ratio of functionalities by the choice of building blocks (*33*). Here we show that incorporation of catalytic cobalt porphyrin (*34*) units into COFs, along with multivariate synthesis of frameworks bearing catalytic cobalt and structural copper units, gives highly active, stable, and selective catalysts for electrochemical reduction of carbon dioxide to carbon monoxide in water. A member of the COF series that we studied exhibits a 26-fold increase in activity compared with the parent molecular precursor and, in many respects, outperforms state-of-the-art molecular and solid-state catalysts, with broad opportunities for further improvement through modular synthesis using appropriate combinations of building units. X-ray absorption measurements reveal that the COF framework can directly influence the electronic structure of the catalytic cobalt centers, in a manner akin to redox noninnocent ligand behavior observed in molecular systems (*35*), thereby contributing to the observed gains in reaction selectivity and activity beyond the steric effects of surface area and site isolation.

We focused our initial electrocatalysis studies on COFs, as we sought to exploit the charge-carrier mobility of these materials derived from π conjugation and π-π stacking (*22*, *36*–*38*), as well as the stability from reticular assembly with strong covalent bonds. We synthesized a model framework (COF-366-Co) by the imine condensation of 5,10,15,20-tetrakis(4-aminophenyl)porphinato]cobalt [Co(TAP)] with 1,4-benzenedicarboxaldehyde (BDA) (Fig. 1). The porous COF material was evacuated by activation with supercritical carbon dioxide and heating to 100°C for 18 hours. The retention of cobalt in the coordinating porphyrin units within the framework was confirmed by elemental analysis (supplementary materials section S1.1), thermogravimetric analysis (fig. S1), and

[1]Department of Chemistry, University of California, Berkeley, CA 94720, USA. [2]Chemical Sciences Division, Lawrence Berkeley National Laboratory, Berkeley, CA 94720, USA. [3]Materials Sciences Division, Lawrence Berkeley National Laboratory, Berkeley, CA 94720, USA. [4]School of Physical Science and Technology, ShanghaiTech University, Shanghai, 201210, China. [5]Department of Materials Science and Engineering, University of California, Berkeley, CA 94720, USA. [6]Kavli Energy Nanoscience Institute, Berkeley, CA 94720, USA. [7]King Fahd University of Petroleum and Minerals, Dhahran 34464, Saudi Arabia. [8]Howard Hughes Medical Institute, University of California, Berkeley, CA 94720, USA. [9]Department of Molecular and Cell Biology, University of California, Berkeley, CA 94720, USA.
*These authors contributed equally to this work. **†Corresponding author. E-mail: yaghi@berkeley.edu (O.M.Y.); chrischang@berkeley.edu (C.J.C.)**

solid-state ultraviolet-visible (UV-Vis) spectroscopy (fig. S3). The formation of the imine linkages in the COF was confirmed by attenuated total reflectance–Fourier transform infrared spectroscopy, which showed the characteristic imine stretching vibration band at 1621 cm^{-1}, as well as the absence of the aldehyde stretching vibration band at 1684 cm^{-1} (fig. S10). The morphologies of the activated COF samples were examined by scanning electron microscopy (SEM), which showed aggregation of only one kind of crystallite of rectangular rod-shaped morphology (~50 nm in length) (Fig. 2A). Powder x-ray diffraction (PXRD) patterns (Fig. 2B) showed intense peaks in the expected low-angle range, with no residual peaks characteristic of the starting materials. To elucidate the constitution of the framework, we used Materials Studio 7.0 to build a structural model (Fig. 1) in an orthorhombic *Cmmm* space group to allow the lattice distortion from regular square nets. Pawley refinements of the PXRD patterns were carried out for full profile fitting against the proposed models, resulting in a good agreement factor (weighted-profile *R* factor R_{wp} = 2.59% and unweighted-profile *R* factor R_p = 1.38% after convergence) and reasonable profile differences. These refinements revealed one-dimensional (1D) channels, 21 Å in width, running along the *c* axis, with a distance of 4.4 Å between the stacking 2D sheets. The porosity and specific surface area were determined using nitrogen adsorption isotherms at 77 K (Fig. 2C). The Brunauer-Emmett-Teller (BET) surface area was determined to be 1360 m^2/g. Density functional theory (DFT) fitting of the adsorption branches showed relatively narrow pore size distributions (10 to 18 Å), in agreement with that of the proposed model.

For electrochemical experiments, the activated microcrystalline COF powders were deposited on porous, conductive carbon fabric. Cyclic voltammetry (CV) measurements on COF-366-Co were conducted in pH 7 aqueous phosphate buffer (Fig. 3A). Under a nitrogen atmosphere, the voltammogram trace shows a departure from the electrode background at about −0.45 V versus a reversible hydrogen electrode (RHE). A broad reduction wave, which was assigned to the Co(II)/Co(I) redox couple, is also apparent at about −0.67 V. The surface concentration of electrochemically active cobalt porphyrin sites was measured by integration of the reduction wave to be 1×10^{-8} mol/cm^2, corresponding to activity at 4% of the cobalt porphyrin sites in the material. The observed continuous current increase at potentials more negative than −0.67 V likely arises from Co(I)-catalyzed proton reduction activity (*39*). After the solution was saturated with carbon dioxide, a substantial current enhancement was observed [catalytic current/noncatalytic current ratio (i_{cat}/i_p) = 1.8 at −0.67 V] (*40*), with a catalytic onset potential at −0.42 V, indicating a prominent catalytic effect of COF-366-Co on the reduction of carbon dioxide in neutral aqueous solution. In contrast, the carbon fabric electrode alone showed minimal current enhancement under a carbon dioxide or nitrogen atmosphere (fig. S56).

In controlled potential electrolyses performed in carbon dioxide–saturated aqueous bicarbonate buffer (pH = 7.3) under applied potentials between −0.57 and −0.97 V (versus RHE), carbon monoxide was observed as the major reduction product (Fig. 3B), with no other detectable carbon-based products. At −0.67 V, which represents an overpotential of −0.55 V, the catalyst displayed optimal performance (figs. S63 and S64). More positive potentials led to sluggish carbon dioxide reactivity, whereas more negative potentials promoted off-pathway water reduction. At −0.67 V, COF-366-Co promoted carbon monoxide evolution at an initial current density of 5 mA per milligram of catalyst (~80 mA per milligram of cobalt), with high selectivity over competing proton reduction [Faradaic efficiency for carbon monoxide (FE_{CO}) = 90%]. Catalytic cobalt porphyrin centers in the COF showed greater than 10% enhancement in carbon dioxide to proton selectivity over the molecular cobalt porphyrin unit alone (Fig. 3B). The catalytic activity of the COF could be maintained for 24 hours, accumulating more than 36 ml of carbon monoxide [standard

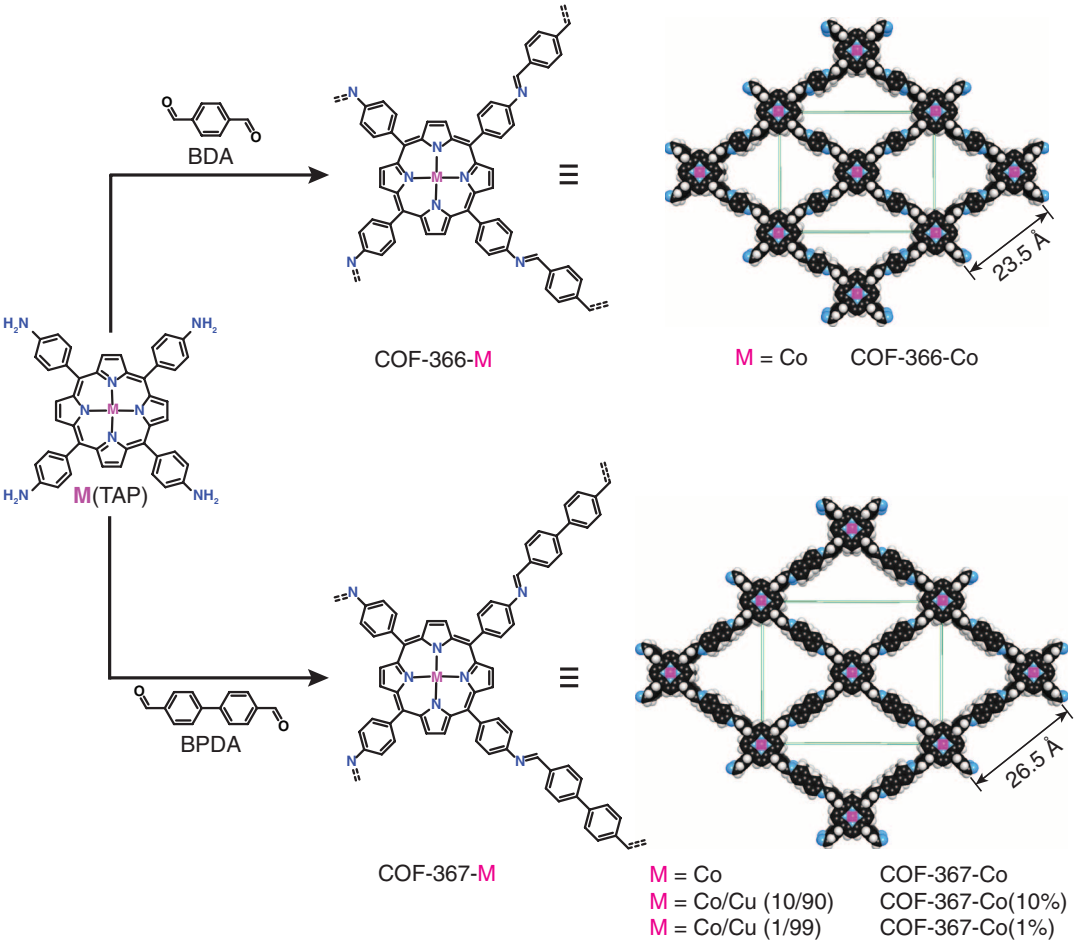

Fig. 1. Design and synthesis of metalloporphyrin-derived 2D covalent organic frameworks. The space-filling structural models of COF-366-M and COF-367-M were obtained using Materials Studio 7.0 and refined with experimental PXRD data.

temperature and pressure (STP), equivalent to 1.6 mmol] per milligram of COF. This corresponds to a turnover number (TON) of 1352 [TON per electroactive cobalt based on the measurements described above (TON_{EA}) ≈ 34,000], with an initial turnover frequency (TOF) of 98 $hour^{-1}$ [TOF per electroactive cobalt (TOF_{EA}) ≈ 2500]. This result represents a substantial improvement over the molecular Co(TAP), which showed an initial TOF of 36 $hour^{-1}$ (TOF_{EA} ≈ 360) and a TON of 794 (TON_{EA} ≈ 8300) after 24 hours of reaction [surface coverage of electroactive sites on a Co(TAP)-modified electrode constitutes ~10% of the total cobalt]. PXRD (fig. S73) and SEM (fig. S74) measurements on the COF catalyst after electrolysis showed neither marked changes in crystallinity and microscopic morphology nor evidence of cobalt nanoparticle formation. By incorporating this molecular unit into a COF scaffold, the resulting hybrid catalyst could be recovered from the electrolysis mixture and reused at least five times without decrease in activity and selectivity (table S8). Control experiments with COFs containing either free-base or copper-metallated porphyrin units, a physical mixture of independently synthesized cobalt nanoparticles (fig. S75) and COF, and Co_3O_4 and related cobalt salts that could be formed as impurities during COF synthesis did not produce appreciable carbon dioxide reduction (fig. S76).

To optimize this carbon dioxide catalyst platform by a modular reticular approach, we prepared the expanded COF-367-Co analog using biphenyl-4,4′-dicarboxaldehyde (BPDA) as the strut in place of BDA (Fig. 1). We reasoned that a larger pore size would allow for higher capacity of carbon dioxide adsorption inside the framework, as well as higher electrochemical and chemical accessibility of the catalytic cobalt porphyrin active sites. COF-367-Co was obtained as a dark purple powder comprising rectangular rod-shaped crystallite aggregates (~100 nm in length) (Fig. 2D). The structural model based on PXRD data and DFT fitting indicated that the constitution and topology of COF-367-Co is analogous to that of COF-366-Co, with the former showing an increased channel width (24 Å) and interlayer distance (4.8 Å) (Fig. 2E). The BET surface area was determined by nitrogen adsorption isotherm (Fig. 2F) as 1470 m^2/g, and pore size distribution was consistent with the model (12 to 23 Å). Cyclic voltammetry studies with COF-367-Co on a carbon fabric electrode in bicarbonate buffer indicated that this extended organic framework exhibits an improved surface concentration (2×10^{-9} mol/cm^2) of electroactive cobalt porphyrin sites over COF-366-Co, which corresponds to accessibility of 8% of the cobalt sites in the bulk material. When the solution was saturated with CO_2, a catalytic current was evident with an onset potential at –0.40 V and a 2.2-fold enhancement at –0.67 V, indicating a prominent effect of COF-367-Co in the catalysis of CO_2 reduction at these potentials (Fig. 3A). As predicted, electrolysis under the same conditions described above revealed that this expanded COF displays improved catalytic efficiency as compared with COF-366-Co. At an applied potential of –0.67 V, COF-367-Co produced more than 100 ml of carbon monoxide (STP, equivalent to 4.5 mmol) per milligram of COF during a 24-hour period (TON = 3901, TON_{EA} ≈ 48,000), with high Faradaic efficiency (91%). The increased TON_{EA} over COF-366-Co indicated that lattice expansion allowed for more efficient exposure of the electroactive sites to the reactants.

In addition to framework expansion, we also sought to optimize catalyst performance by introducing building-block heterogeneity through a multivariate strategy (*33*), as we hypothesized that not all electroactive cobalt porphyrin sites in the material fully participated in electrocatalysis, owing to the low aqueous solubility of carbon dioxide. Specifically, we reasoned that using isostructural metalloporphyrin units that are catalytically inactive for carbon dioxide reduction (fig. S76) to dilute electroactive cobalt porphyrin active sites within the extended lattice could increase the proportion of the active sites exposed to the reactant and thereby improve the turnover frequency on a per-cobalt basis. Copper porphyrin was chosen for this study, as the corresponding COF-367-Cu had the highest surface area among all analogous COF-367-M (M = Ni, Zn, H_2) synthesized. The resulting bimetallic COF-367 derivatives, termed COF-367-Co(10%) and COF-367-Co(1%), were prepared; the numbers in the parentheses indicate the proportion of cobalt in all metal sites (Fig. 1). Inductively coupled plasma

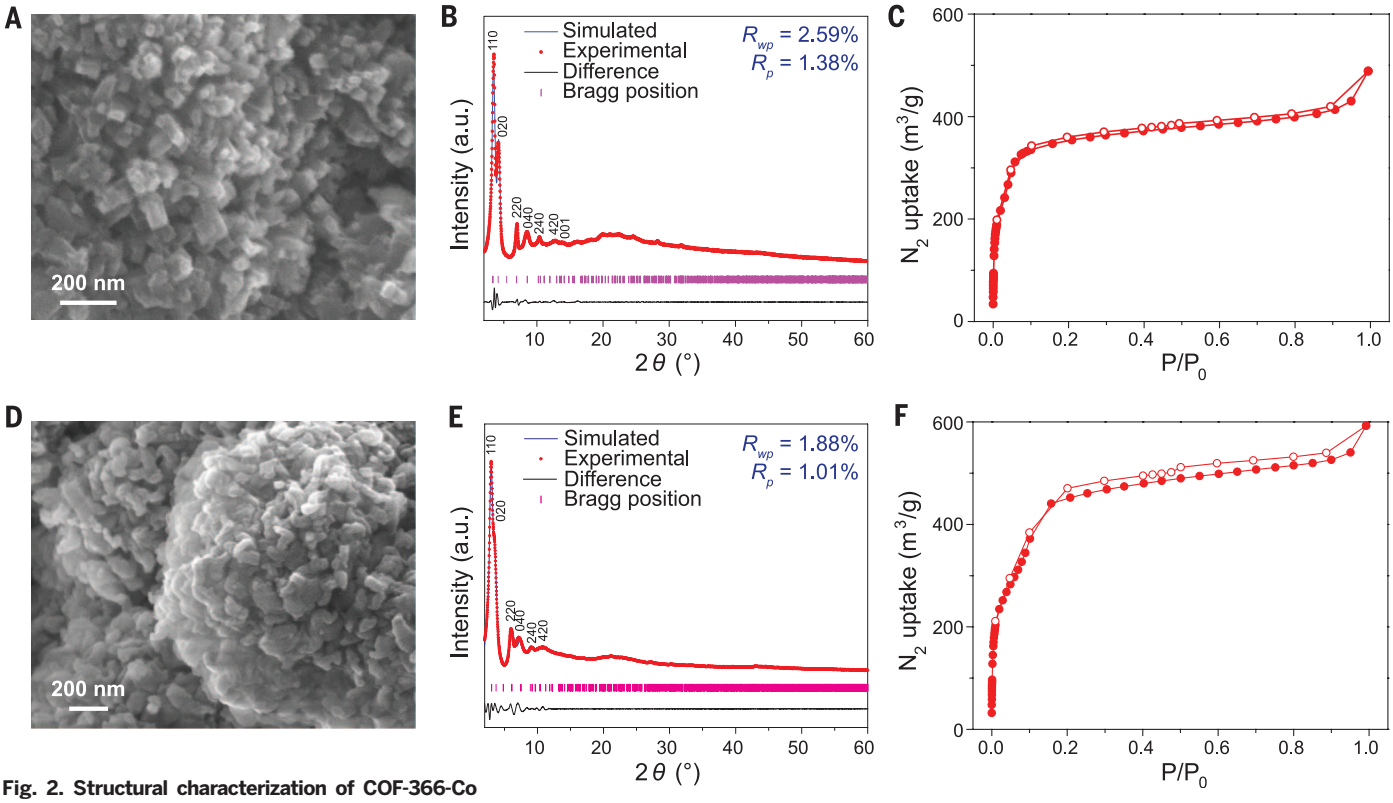

Fig. 2. Structural characterization of COF-366-Co and COF-367-Co. (**A**) SEM image of COF-366-Co. (**B**) Experimental (red line) and simulated (blue line) PXRD patterns of COF-366-Co. a.u., arbitrary units. (**C**) Nitrogen adsorption isotherm for COF-366-Co. P, pressure of the system; P_0, saturation pressure. (**D**) SEM image of COF-367-Co. (**E**) Experimental (red line) and simulated (blue line) PXRD patterns of COF-367-Co. (**F**) Nitrogen adsorption isotherm for COF-367-Co.

(ICP) analyses confirmed that the final chemical composition of the COFs obtained reflected the initial ratio of the two metalloporphyrin starting materials that we used (supplementary materials section S1.1). The TOF per electroactive cobalt site for carbon monoxide production in these multivariate Co/Cu COF-367 catalysts showed a substantial improvement with each 10-fold dilution of cobalt loading. The average TOF per active cobalt for the first 4 hours of reaction was measured as follows: COF-367-Co, 165 hour^{-1} (TOF_{EA} ≈ 1900); COF-367-Co(10%), 360 hour^{-1} (TOF_{EA} ≈ 4400); and COF-367-Co(1%), 764 hour^{-1} (TOF_{EA} ≈ 9400) (Fig. 3C). The TOF_{EA} values were roughly estimated, assuming that all three frameworks had comparable percentages of electroactive sites (8%). Although the low cobalt concentration in COF-367-Co(10%) and COF-367-Co(1%) hampered the accurate determination of the surface concentration of electrochemically accessible cobalt sites by CV, the bimetallic frameworks had nearly identical pore sizes, interlayer distances, and surface areas to the parent COF-367-Co on the basis of PXRD and nitrogen adsorption measurements (figs. S25 and S32 to S43), which suggests that such an assumption may be valid. Owing to the moderate

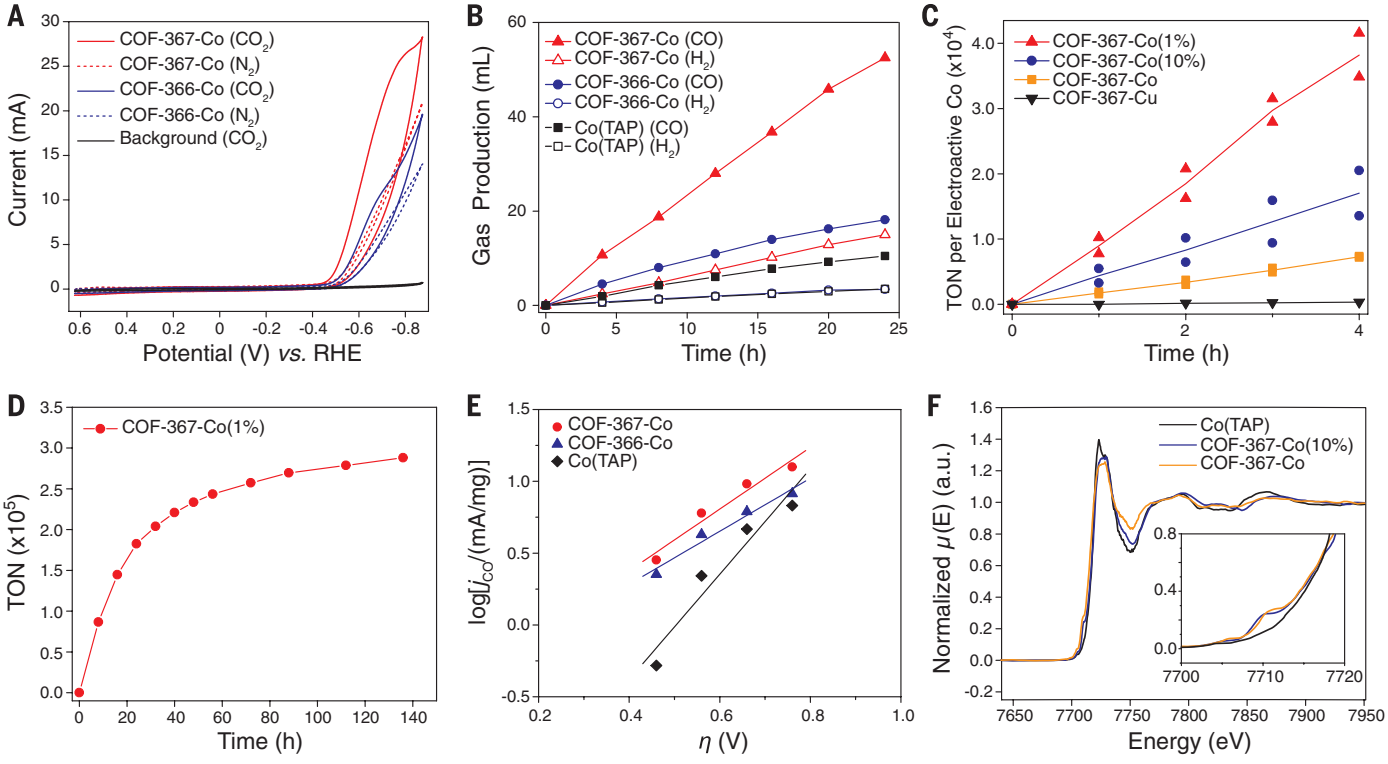

Fig. 3. Electrochemical and spectroelectrochemical characterizations and carbon dioxide reduction performance of the COFs. (**A**) Cyclic voltammograms of COF-366-Co and COF-367-Co in carbon dioxide–saturated medium (blue and red solid lines, respectively) or nitrogen-saturated medium (blue and red dotted lines, respectively). The black solid line shows background (bare carbon electrode) CV responses in carbon dioxide–saturated medium. The medium was pH 7.2 aqueous potassium phosphate buffer (0.2 M) with additives: 0.5 M $KHCO_3$ under carbon dioxide atmosphere to maintain a neutral pH, or 0.5 M $NaClO_4$ under nitrogen atmosphere to match the ionic strength. (**B**) Long-term bulk electrolyses at −0.67 V (versus RHE), showing the volume of carbon monoxide produced by COF-367-Co (red solid triangles), COF-366-Co (blue solid circles), or Co(TAP) (black solid squares) and the volume of hydrogen produced by COF-367-Co (red open triangles), COF-366-Co (blue open circles), or Co(TAP) (black open squares). (**C**) Bulk electrolyses of bimetallic COFs at −0.67 V (versus RHE), showing TON of carbon monoxide production by COF-367-Co(1%) (red solid triangles), COF-367-Co(10%) (blue solid circles), COF-367-Co (orange solid squares), or COF-367-Cu (purple solid inverted triangle; TON with respect to the amount of copper porphyrin). Two separate experimental runs were conducted for each time point, with the line showing the average of the measurements. (**D**) Long-term bulk electrolysis of COF-367-Co(1%) at −0.67 V (versus RHE). (**E**) Tafel plots of electrolysis using COF-367-Co (red solid circles), COF-366-Co (blue solid triangles), or Co(TAP) (black solid diamonds), showing only the linear, low–current density regime where the reaction rate is not limited by mass transport. (**F**) X-ray absorption spectra of COF-367-Co (orange line), COF-367-Co(10%) (blue line), and Co(TAP) (black line). The inset shows the pre-edge regime of the same spectra. (**G**) Spectroelectrochemical data using in situ UV-Vis, showing the steady-state relative absorbance at different applied potentials (0.23 to −0.57 V versus RHE) with reference to that at 0.33 V. (**H**) Time dependence of the relative UV-Vis absorbance at 640-nm wavelength at −0.57 V, with respect to the steady-state UV-Vis absorbance at 640 nm at 0.33 V. Potential is applied at 4 s. Linear regression yielded the apparent diffusion coefficient (D_{app}) according to a modified Cottrell equation: $\Delta Absorption = \frac{2A_{max}D_{app}^{1/2}t^{1/2}}{d\pi^{1/2}}$ (fig. S81) (*47*). Here, A_{max} is the maximum absorption of the thin films at 640 nm, d is the overall thickness of the thin films, and t is time.

proton reduction ability of the copper porphyrin sites in the hybrid organic framework, the TOF increased as the Co/Cu ratio decreased, at the expense of Faradaic efficiency for carbon monoxide production [FE_{CO} = 70% for COF-367-Co(10%) and 40% for COF-367-Co(1%)]. In a long-term electrolysis experiment (Fig. 3D), COF-367-Co (1%) displayed a TON of > 24,000 ($TON_{EA} \approx$ 296,000), which indicates that it is one of the most efficient electrochemical carbon dioxide reduction catalysts reported to date (*3*, *4*). The observed activity enhancements for the bimetallic COFs are due to their multivariate nature; indeed, the analogous physical mixture of COF-367-Co and COF-367-Cu in a 1:9 ratio produced far less carbon dioxide reduction activity compared with COF-367-Co(10%) (table S17).

In addition to challenges posed by the low aqueous solubility and limited diffusion of CO_2 within the COF, only a small portion (4 to 8%) of the cobalt centers in the COF material deposited in this manner proved to be electroactive, presumably because of the limited electrochemical contact between the COF powder and the electrode (*41*). As such, we explored the possibility of growing COF directly onto the surface of an electrode substrate in the form of oriented thin films (*42*–*44*). Layers of COF sheets could be successfully synthesized directly on glassy carbon, fluorine-doped tin oxide (FTO), and silicon oxide. Grazing-incidence wide-angle x-ray scattering (GIWAXS) patterns showed the formation of highly crystalline COF thin films (figs. S48 to S51) (*45*). With the use of ICP, the concentration of COF on the substrate surface was determined to be 1.3×10^{-5} mmol Co per square centimeter, corresponding to a thickness of ~350 nm, which is consistent with images obtained by cross-sectional SEM (figs. S54 and S55). The charge transport through the COF-366-Co thin films was characterized using spectroelectrochemistry. Under an applied potential more negative than –0.37 V in nitrogen- or carbon dioxide–saturated pH 7 aqueous buffer, the UV-Vis spectrum of the FTO-supported COF underwent changes attributable to Co(II)/Co(I) reduction (Fig. 3G and figs. S78 to S82). Using the steady-state spectroscopic response to the reduction potentials in combination with the Nernst equation, the redox potential ($E_{1/2}$) could be estimated to be more negative than –0.52 V (fig. S83), in agreement with the CV measurements ($E_{1/2} \approx$ –0.67 V) (*46*). The time-dependence of the UV-Vis response of a COF-coated FTO electrode to an applied potential of –0.57 V was studied in a CO_2-saturated $KHCO_3$ solution (Fig. 3G), and a fit of the data to a modified Cottrell equation afforded an apparent diffusion coefficient of 2×10^{-12} cm^2/s (fig. S81), a value substantially higher than that obtained with analogous metal-organic framework (MOF) thin films bearing cobalt porphyrin units (*47*). Using the silicon oxide–hosted sample, we measured the direct current conductivity of COF-366-Co to be ~10^{-6} S/cm, which is also higher than that of the MOF (figs. S84 and S85). In addition to a presumably increased portion of electroactive cobalt sites, the favorable charge-transport properties led to a higher catalytic efficiency. Under the same electrolysis conditions, COF-366-Co thin films on glassy carbon exhibited a TOF of 665 $hour^{-1}$, a value seven times as high as that of the same material deposited on a carbon fabric, with a high current density of 45 mA/mg and a Faradaic efficiency of 86%.

Electrokinetics experiments indicated that covalently linking cobalt porphyrin active sites within a COF influences the mechanistic pathways for carbon dioxide reduction. For the systems employing COF-366-Co, COF-367-Co, and COF-367-Co(10%), Tafel plots of the logarithm of current density [$\log(j_{CO})$] versus the overpotential (η) display comparable slopes between 470 and 550 mV/dec (where 1 dec is one order of magnitude) in the linear, lower–current density regime (–0.57 to –0.87 V). This result differs considerably from what is observed for the molecular Co(TAP) analog (270 mV/dec) (Fig. 3E and figs. S65 to S68). This difference suggests that, when embedded in a structurally and electronically extended framework, cobalt porphyrin catalyzes carbon dioxide reduction by a different mechanism than that which pertains with the simple molecular analog. In addition, both the COF and Co(TAP) catalysts showed a first-order rate dependence on the partial pressure of carbon dioxide (fig. S87) and no rate dependence on the pH (figs. S88 and S89), indicating that the rate-limiting chemical step involves the participation of one molecule of carbon dioxide and no proton.

Finally, we applied x-ray absorption spectroscopy (XAS) as a probe to evaluate how the surrounding COF influenced the electronic structures of incorporated catalytic cobalt porphyrin units and, in turn, the associated carbon dioxide reduction mechanism (*48*, *49*). Comparison of the cobalt K-edge XAS spectra of Co(TAP), COF-367-Co, and COF-367-Co(10%) (Fig. 3F) reveals a similar line size, shape, and position, consistent with a formal Co(II) oxidation state for all samples. When a reduction potential (–0.67 V) was applied to COF-367-Co under a carbon dioxide atmosphere, the K-edge revealed a line-shape change consistent with the partial reduction of Co(II) to Co(I) (fig. S96). The two COF catalysts also exhibited an additional pre-edge feature not present in the molecular Co(TAP) analog (Fig. 3F, inset); this difference shows that the COF environment could directly modulate the electronic properties of molecular centers coupled into the extended lattice (*50*, *51*). This feature, unique to the COFs, was also observed when the catalysts were subjected to open-circuit or electrolysis (–0.67 V) potentials in a bicarbonate buffer (figs. S92 to S95). The communication between the metal and COF lattice could furnish a cobalt center with a more delocalized electronic structure, a network-solid analog to noninnocent ligand behavior in molecular systems (*35*).

Incorporating tunable molecular units within an extended COF thus gives rise to electrocatalysts that display advantageous features of both molecular and heterogeneous systems and promote carbon dioxide reduction to carbon monoxide with exceptionally high activity and selectivity compared with existing systems (table S21). We anticipate that these hybrid molecular-material platforms will be applicable to a broad range of catalytic applications, particularly those that require sustainable electrical and/or solar input and aqueous compatibility.

REFERENCES AND NOTES

1. N. S. Lewis, D. G. Nocera, *Proc. Natl. Acad. Sci. U.S.A.* **103**, 15729–15735 (2006).
2. H. B. Gray, *Nat. Chem.* **1**, 7 (2009).
3. C. Costentin, M. Robert, J.-M. Savéant, *Chem. Soc. Rev.* **42**, 2423–2436 (2013).
4. B. Kumar *et al*., *Annu. Rev. Phys. Chem.* **63**, 541–569 (2012).
5. A. M. Appel *et al*., *Chem. Rev.* **113**, 6621–6658 (2013).
6. B. Fisher, R. Eisenberg, *J. Am. Chem. Soc.* **102**, 7361–7363 (1980).
7. J. Hawecker, J.-M. Lehn, R. Ziessel, *J. Chem. Soc. Chem. Commun.* **1984**, 328–330 (1984).
8. M. Beley, J. P. Collin, R. Ruppert, J. P. Sauvage, *J. Am. Chem. Soc.* **108**, 7461–7467 (1986).
9. E. B. Cole *et al*., *J. Am. Chem. Soc.* **132**, 11539–11551 (2010).
10. M. Bourrez, F. Molton, S. Chardon-Noblat, A. Deronzier, *Angew. Chem. Int. Ed.* **50**, 9903–9906 (2011).
11. J. Schneider *et al*., *Energy Environ. Sci.* **5**, 9502–9510 (2012).
12. V. S. Thoi, N. Kornienko, C. G. Margarit, P. Yang, C. J. Chang, *J. Am. Chem. Soc.* **135**, 14413–14424 (2013).
13. P. Kang, T. J. Meyer, M. Brookhart, *Chem. Sci.* **4**, 3497–3502 (2013).
14. B. A. Rosen *et al*., *Science* **334**, 643–644 (2011).
15. K. P. Kuhl, E. R. Cave, D. N. Abram, T. F. Jaramillo, *Energy Environ. Sci.* **5**, 7050–7059 (2012).
16. C. W. Li, M. W. Kanan, *J. Am. Chem. Soc.* **134**, 7231–7234 (2012).
17. W. Zhu *et al*., *J. Am. Chem. Soc.* **135**, 16833–16836 (2013).
18. D. Kim, J. Resasco, Y. Yu, A. M. Asiri, P. Yang, *Nat. Commun.* **5**, 4948 (2014).
19. S. Zhang, P. Kang, T. J. Meyer, *J. Am. Chem. Soc.* **136**, 1734–1737 (2014).
20. A. P. Côté *et al*., *Science* **310**, 1166–1170 (2005).
21. E. L. Spitler, W. R. Dichtel, *Nat. Chem.* **2**, 672–677 (2010).
22. S. Wan *et al*., *Chem. Mater.* **23**, 4094–4097 (2011).
23. H. M. El-Kaderi *et al*., *Science* **316**, 268–272 (2007).
24. E. L. Spitler *et al*., *Angew. Chem. Int. Ed.* **51**, 2623–2627 (2012).
25. W. Lu *et al*., *Chem. Soc. Rev.* **43**, 5561–5593 (2014).
26. D. N. Bunck, W. R. Dichtel, *Angew. Chem. Int. Ed.* **51**, 1885–1889 (2012).
27. L. Ma, J. M. Falkowski, C. Abney, W. Lin, *Nat. Chem.* **2**, 838–846 (2010).
28. J. Lee *et al*., *Chem. Soc. Rev.* **38**, 1450–1459 (2009).
29. J. Park, D. Feng, H.-C. Zhou, *J. Am. Chem. Soc.* **137**, 1663–1672 (2015).
30. D. J. Xiao *et al*., *Nat. Chem.* **6**, 590–595 (2014).
31. C. Wang, Z. Xie, K. E. deKrafft, W. Lin, *J. Am. Chem. Soc.* **133**, 13445–13454 (2011).
32. S. Pullen, H. Fei, A. Orthaber, S. M. Cohen, S. Ott, *J. Am. Chem. Soc.* **135**, 16997–17003 (2013).
33. H. Deng *et al*., *Science* **327**, 846–850 (2010).
34. D. Behar *et al*., *J. Phys. Chem. A* **102**, 2870–2877 (1998).
35. R. Eisenberg, H. B. Gray, *Inorg. Chem.* **50**, 9741–9751 (2011).
36. G. H. V. Bertrand, V. K. Michaelis, T. C. Ong, R. G. Griffin, M. Dincă, *Proc. Natl. Acad. Sci. U.S.A.* **110**, 4923–4928 (2013).
37. J. Guo *et al*., *Nat. Commun.* **4**, 2736 (2013).
38. M. Calik *et al*., *J. Am. Chem. Soc.* **136**, 17802–17807 (2014).
39. In pH 7.2 phosphate buffer, electrolyses at potentials equal to or more negative than –0.67 V resulted in moderate hydrogen evolution reactivity. However, this activity was largely suppressed when the solution was saturated with carbon dioxide (see below).
40. The intrinsic i_{cat}/i_p value was likely higher, as under carbon dioxide atmosphere, the current resulting from proton reduction was inhibited.
41. C. R. DeBlase *et al*., *ACS Nano* **9**, 3178–3183 (2015).
42. J. W. Colson *et al*., *Science* **332**, 228–231 (2011).
43. D. D. Medina *et al*., *ACS Nano* **8**, 4042–4052 (2014).
44. X.-H. Liu *et al*., *J. Am. Chem. Soc.* **135**, 10470–10474 (2013).
45. The COF-coated glassy carbon showed an ill-defined GIWAXS pattern due to high background scattering (figs. S52 and S53). Because the synthetic conditions were identical to those used with FTO and silicon oxide, we assumed that the COF grown on glassy carbon also formed a crystalline thin film.
46. $E_{1/2}$ could not be accurately measured with this method, owing to decomposition of FTO at potentials more negative than –0.57 V.
47. S. R. Ahrenholtz, C. C. Epley, A. J. Morris, *J. Am. Chem. Soc.* **136**, 2464–2472 (2014).
48. A. A. Peterson, J. K. Nørskov, *J. Phys. Chem. Lett.* **3**, 251–258 (2012).

49. N. Kornienko *et al.*, *J. Am. Chem. Soc.* **137**, 7448–7455 (2015).
50. F. de Groot, G. Vankó, P. Glatzel, *J. Phys. Condens. Matter* **21**, 104207 (2009).
51. J. Yano *et al.*, *Science* **314**, 821–825 (2006).

ACKNOWLEDGMENTS

Financial support for energy catalysis in the C.J.C. laboratory was provided by U.S. Department of Energy (DOE)/Lawrence Berkeley National Laboratory (LBNL) grant 101528-002. Financial support for COF research in the O.M.Y. laboratory was provided by BASF SE (Ludwigshafen, Germany) for synthesis and by DOE, Office of Science, Office of Basic Energy Sciences, Energy Frontier Research Center grant DESC0001015 for adsorption and multivariate metallation. Financial support for energy catalysis in the P.Y. laboratory was supported by the Director of the Office of Science, Office of Basic Energy Sciences, Materials Science and Engineering Division, DOE, under contract no. DE-AC02-05CH11231(Surface). E.M.N. acknowledges the NSF Graduate Research Fellowships Program for a predoctoral fellowship. A.R.P. acknowledges the Amgen Scholar Program for support of undergraduate summer research. We thank C. Canlas (University of California, Berkeley) for the acquisition of solid-state nuclear magnetic resonance spectra and C. Zhu at the Advanced Light Source (ALS) at LBNL for the acquisition of GIWAXS data. XAS measurements were performed at the ALS. The ALS is an Office of Science user facility operated by LBNL for the DOE, Office of Science, and supported by the DOE under contract no. DE-AC02-05CH11231. We are indebted to Prince Dr. Turki bin Saud bin Mohammed Al-Saud, King Abdulaziz City for Science and Technology (Saudi Arabia), for valuable discussions concerning carbon capture and utilization applications.
The data reported in the paper are presented in the supplementary materials.

SUPPLEMENTARY MATERIALS

www.sciencemag.org/content/349/6253/1208/suppl/DC1
Materials and Methods
Figs. S1 to S96
Tables S1 to S21
References (*52*–*72*)

19 June 2015; accepted 5 August 2015
Published online 20 August 2015
10.1126/science.aac8343

GEOPHYSICS

Stress orientations in subduction zones and the strength of subduction megathrust faults

Jeanne L. Hardebeck

Subduction zone megathrust faults produce most of the world's largest earthquakes. Although the physical properties of these faults are difficult to observe directly, their frictional strength can be estimated indirectly by constraining the orientations of the stresses that act on them. A global investigation of stress orientations in subduction zones finds that the maximum compressive stress axis plunges systematically trenchward, consistently making an angle of 45° to 60° with respect to the subduction megathrust fault. These angles indicate that the megathrust fault is not substantially weaker than its surroundings. Together with several other lines of evidence, this implies that subduction zone megathrusts are weak faults in a low-stress environment. The deforming outer accretionary wedge may decouple the stress state along the megathrust from the constraints of the free surface.

Subduction zones pose a considerable hazard as the main source of great earthquakes (magnitude ≥8). Relative to other fault types, subduction zone megathrust faults may also have unique physical properties, due to the sediments and fluids that are entrained by the subducting oceanic plate (*1*). The presence of fluids, particularly at high fluid pressures, can weaken faults substantially (*2*). Direct evidence suggests that subduction zone megathrust faults slip with low frictional resistance near Earth's surface (*3*). The strength of these faults at seismogenic depths is less clear, as they can only be studied indirectly.

The orientation of a fault with respect to the stress field can be an indicator of the fault's strength. Faults optimally oriented for frictional failure make an angle of ~30° to the maximum compressive stress axis, σ_1. Nonoptimally oriented faults can also be active, but faults with typical frictional strength should not slip at a high angle to σ_1 (≥60°) (*4*). Faults operating at a high angle to σ_1 must be very weak compared to the surrounding material to slip at relatively low applied shear stress. Similarly, faults oriented at a very low angle to σ_1 (<10°) must also be weak.

The traction at Earth's surface is zero, requiring an Andersonian stress state in which one principal stress axis is vertical (*5*). Most crustal faulting is consistent with an Andersonian stress state (*6*). The very shallow dip (~10°) of the upper portion of many subduction zone megathrusts (*7*) suggests that, if these faults exist within an Andersonian stress state, they operate at a high angle to one principal stress axis (and at a low angle to the other two) and are therefore frictionally weak. However, observations from some subduction zone locations indicate that the stress in these locations is not Andersonian (*8*–*11*).

I systematically investigate the stress orientations in subduction zones worldwide, to determine whether the stress state is generally non-Andersonian and whether megathrust faults are well-oriented for failure. I compile the moment tensors (*12*, *13*) of earthquakes located within 20 km of the subduction zone interface (*7*) to represent the megathrust region, and more shallow events to represent the upper plate. I stack the events for each subduction zone to invert for stress orientation (*14*) as a one-dimensional function of subduction interface depth. For the several subduction zones near Japan, there are enough moment tensors to invert for the two-dimensional spatially varying stress field as well.

The stress state in the subduction zones near Japan is generally not Andersonian. The σ_1 axis in most megathrust regions plunges systematically trenchward (opposite the direction of subduction zone dip), generally plunging between 10° and 50° (Fig. 1A). A similar plunge of the σ_1 axis is observed within the upper plate above the Japan Trench, Kuril Trench, and Nankai Trough (Fig. 1G), whereas back-arc extension (near-vertical σ_1) dominates above the Ryukyu and Izu-Bonin trenches.

Comparing the plunge of the σ_1 axis in the megathrust region to the dip of the subduction interface (*7*) gives the angle of σ_1 to the megathrust fault (Fig. 1B). For the Kuril, Japan, and Izu-Bonin trenches, the σ_1 axis is typically at an angle of 20° to 50° to the fault. For the Ryukyu Trench, the σ_1 axis makes somewhat larger angles of 30° to 80° to the fault. In the Nankai Trough, σ_1 is oriented at 10° to 30° to the fault in the upper 20 km, while at deeper depths, the σ_1 axis is near-vertical. The plunge of the σ_1 axis is stable with depth (Fig. 1C), except in the Nankai Trough (Fig. 1D), and the subduction megathrust is generally well oriented for failure from the near-surface to at least 60 km depth (Fig. 1E). The stacked Kuril, Japan, and Izu-Bonin trenches (the subducting Pacific plate) show a megathrust fault that is optimally oriented for failure, at ~30° to σ_1, over the full depth range. The megathrust at the Ryukyu Trench is generally well oriented for failure at <60° down to 30 km depth, and is marginally oriented at ~60° from 30 km to 60 km depth. The exception is the Nankai Trough (Fig. 1F), which is well oriented at ~20° to σ_1 only in the upper 20 km. Below 30 km, the megathrust is not oriented for reverse faulting within the error bounds. This suggests that 30 km is the downward limit of coupling between the subducting and overriding plates.

For all global subduction zones studied, for almost all depths, the σ_1 axis plunges systematically trenchward, with plunge generally between 10° and 50° (Fig. 2A). The plunge tends to decrease with depth, while the subduction zone dip increases (*7*), so that the angle of σ_1 to the subduction interface is remarkably stable with depth (Fig. 2B). This angle is also remarkably similar across subduction zones, most falling within the range 45° to 60°.

The Japan and South American subduction zones are anomalous in being more optimally

U.S. Geological Survey, Menlo Park, CA, USA.
E-mail: jhardebeck@usgs.gov

Covalent organic frameworks comprising cobalt porphyrins for catalytic CO_2 reduction in water

Song Lin *et al.*

Science **349**, 1208 (2015);
DOI: 10.1126/science.aac8343